

1 Stable and low photovoltage loss perovskite solar cells by multifunctional
2 passivation

3 Guang Yang^{1,2,13}, Zhiwei Ren^{1,13}, Kuan Liu^{1,13}, Minchao Qin⁴, Wanyuan Deng^{1,5},
4 Hengkai Zhang¹, Haibing Wang², Jiwei Liang², Feihong Ye², Qiong Liang¹, Hang
5 Yin⁸, Yuxuan Chen⁹, Yuanlin Zhuang², Siqi Li⁷, Bawei Gao⁶, Jianbo Wang², Tingting
6 Shi¹⁰, Xin Wang⁹, Xinhui Lu⁴, Hongbin Wu⁵, Jianhui Hou⁶, Dangyuan Lei^{7,11}, Shu
7 Kong So⁸, Yang Yang^{3†}, Guojia Fang^{2†}, Gang Li^{1,12†}

8 **Affiliations:**

9 ¹Department of Electronic and Information Engineering, Research Institute for Smart
10 Energy (RISE), The Hong Kong Polytechnic University, Hung Hom, Kowloon, Hong
11 Kong, China

12 ²Key Laboratory of Artificial Micro/Nano Structures of Ministry of Education, School
13 of Physics and Technology, Wuhan University, Wuhan 430072, China

14 ³Department of Materials Science and Engineering and California NanoSystems
15 Institute, University of California, Los Angeles, California 90095, United States

16 ⁴Department of Physics, The Chinese University of Hong Kong, New
17 Territories, Hong Kong, China

18 ⁵Institute of Polymer Optoelectronic Materials and Devices, State Key Laboratory of
19 Luminescent Materials and Devices, South China University of Technology,
20 Guangzhou, China

21 ⁶Institute of Chemistry, Chinese Academy of Sciences, Beijing, China

22 ⁷Department of Applied Physics, The Hong Kong Polytechnic University, Hung Hom,
23 Kowloon, Hong Kong, China

28 ⁸Department of Physics and Institute of Advanced Materials, Hong Kong Baptist
29 University, Kowloon Tong, Hong Kong SAR, P. R. China

30 ⁹South China Academy of Advanced Optoelectronics, South China Normal University,
31 Guangzhou 510006, China

32 ¹⁰Siyuan Laboratory, Guangzhou Key Laboratory of Vacuum Coating Technologies
33 and New Energy Materials, Department of Physics, Jinan University, Guangzhou
34 510632, China

35 ¹¹Department of Materials Science and Engineering, City University of Hong Kong,
36 Kowloon, 999077, Hong Kong, China

37 ¹²The Hong Kong Polytechnic University Shenzhen Research Institute, Shenzhen
38 518057, China

39 ¹³These authors contributed equally: Guang Yang, Zhiwei Ren and Kuan Liu.

40 †Correspondence to: email: gang.w.li@polyu.edu.hk; gjfang@whu.edu.cn;
41 yangy@ucla.edu

42
43
44
45
46

47 **Abstract:** Metal halide perovskite solar cells (PSCs) have demonstrated high power
48 conversion efficiency (PCE), while further efficiency enhancement requires reducing
49 bandgap-voltage offset (W_{OC}) and non-radiative recombination photovoltage loss
50 ($\Delta V_{OC,nr}$). Here, we report an effective approach in reducing the photovoltage loss
51 through the simultaneous (a) internal bulk defects and (b) dimensionally graded 2D
52 perovskite interface defects passivation. Through this Dimensionally Graded
53 Perovskite Formation (DGPF) approach, an open-circuit voltage (V_{OC}) of 1.24 V was
54 obtained with a champion PCE of 21.54% in a 1.63 electron volts (eV) perovskite
55 system (maximum V_{OC} =1.25 V, W_{OC} =0.38 V, and $\Delta V_{OC,nr}$ =0.10 V); we further
56 decreased W_{OC} to 0.326 V in a 1.53 eV perovskite system with a V_{OC} of 1.21 V and a
57 PCE of 23.78% (certified 23.09%). This approach is equally effective in achieving
58 low W_{OC} ($\Delta V_{OC,nr}$) in 1.56 eV and 1.73 eV PSC systems, and further leads to
59 significantly improved operational stability of PSCs.

60

61 **Introduction**

62 Perovskite solar cells (PSCs) based on three-dimensional (3D) perovskite absorbers
63 have achieved rapid progress with power conversion efficiency (PCE) of over 25%, due
64 to the outstanding optoelectronic properties of 3D perovskites. Nevertheless, their poor
65 stability nature, particularly the susceptibility to humid environments, lack of thermal
66 stability, and light-soaking degradation, become a major shortcoming that limits their
67 further practical application.

68 As PSCs' band gap-voltage offset (W_{OC}) is still higher than GaAs (W_{OC} ~0.3 V)
69 cells¹, reducing the W_{OC} and pushing the PSCs' V_{OC} towards the Schottky-Queisser
70 V_{OC} limit (radiative recombination loss only) is of great significance in boosting the
71 PCE as well as understanding the fundamental science^{2,3,4,5,6}. Several studies have
72 shown that non-radiative recombination via defects at the interfaces between
73 perovskite and charge transport layers are the main sources of voltage losses for
74 PSCs^{7,8,9}. Strategies such as surface passivation or processing additives have been
75 explored to minimize the non-radiative recombination losses at interfaces and thus to

76 improve the V_{OC} of devices^{10, 11}. For example, surfaces and grain boundaries with
77 potassium passivation was shown to enable substantial mitigation of non-radiative
78 recombination losses ($\Delta V_{OC,nr}$), pushing the V_{OC} up to 1.17 V with a low W_{OC} of 0.39
79 V ($\Delta V_{OC,nr} = 0.11$ V) for a 1.56-eV-bandgap 3D perovskite system. However, there are
80 still substantial non-radiative losses causing from trap states within the perovskite
81 bulk film, which limits the performance and stability of perovskite devices¹². In
82 addition, the energy level alignment at the interface is also a key factor for
83 minimizing interfacial non-radiative recombination, which requires careful interface
84 design¹³. Thus, simultaneous interface and bulk trap passivation strategy as well as
85 interface engineering are required to further reach the full thermodynamic potential of
86 V_{OC} .

87 In this work, we introduced a multifunctional (bulk and interface) 2D perovskite
88 passivation approach and graded interface design to significantly reduce PSC
89 photovoltage loss and enhance device stability. N-butylammonium bromide (BABr)
90 was first coated on top of the 3D perovskite film, and through thermal driving, we
91 simultaneously achieved relatively uniform distribution of self-passivated 2D/3D
92 perovskites in the bulk, covered by graded mixed dimensional, wider bandgap 2D
93 perovskite layers. We name it as Dimensionally Graded Perovskite Formation (DGPF)
94 approach. This multifunctional approach effectively suppresses the non-radiative
95 recombination loss in both the bulk and the interface of perovskite. Via this DGPF
96 technique, we demonstrate a hysteresis-free maximum PCE of 21.54% with a high
97 V_{OC} of 1.24 V in a 1.63 eV perovskite system, and the W_{OC} is only 0.39 V, equivalent
98 to non-radiative recombination V_{OC} loss ($\Delta V_{OC,nr}$) of only 0.11 V. Particularly,
99 minimum W_{OC} of 0.38 V and $\Delta V_{OC,nr}$ of 0.10 V was achieved in a 20.15% PCE device.
100 We further decrease the W_{OC} as low as 0.326 V in a \sim 1.53 eV perovskite system
101 ($\Delta V_{OC,nr} = 74$ mV), with a maximum V_{OC} of 1.21 V and champion PCE of 23.78%
102 (certified PCE of 23.09%). The DGPF approach is also validated by examining hybrid
103 PSCs with bandgaps of 1.56 eV and 1.73 eV, where very low W_{OC} ($\Delta V_{OC,nr}$) and high
104 V_{OC} were both achieved. At the same time, the 2D perovskite components in the bulk
105 and at the interface provide superb stability under illumination, ensuring the DGPF

106 device can maintain 91% of its initial efficiency over 500 h under 1-sun illumination
107 at MPP condition.

108 Fig. 1a shows the schematic illustration of our DGPF method, and Fig. 1b shows
109 the cross-sectional high-resolution transmission electron microscope (HRTEM) of the
110 DGPF perovskite film deposited on the SnO₂-coated ITO substrate, which can verify
111 the homogeneity of 2D perovskite layer on the top of 3D perovskite films¹⁴. The 3D
112 perovskite films with a quaternary-cation of RbCsMAFA was formed by using the
113 antisolvent-assisted one-step method¹⁵, which has demonstrated state-of-the-art
114 device performances in several studies from EPFL team^{15, 16, 17}. The quaternary-cation
115 perovskite system has shown not only high efficiency, but also higher V_{OC} (1.16-1.18
116 V) than ternary-cation (~1.13 V) counterpart (both are ~1.63 eV bandgap)^{15, 16, 17}. The
117 detailed fabrication method of the device is given in the Experimental Section. Here,
118 to form a mixed 2D/3D perovskite heterojunction films, long-chain
119 n-Butylammonium bromide (BABr) molecules were first dissolved in isopropyl
120 alcohol (IPA) with different concentrations, and then directly spin-coated to form a
121 thin film on top of the as-prepared 3D RbCsMAFA perovskite films, which was
122 followed by thermal annealing at 100°C for 10 min. This approach leads to perovskite
123 vertical composition distribution evidenced below.

124 To investigate the distribution of ions inside the perovskite films after introducing
125 BABr, we conducted time-of-flight secondary ion mass spectrometry (ToF-SIMS)
126 measurement on the DGPF perovskite films. ToF-SIMS depth profile shown in Fig.
127 1c reveals that a gradient distribution of BA⁺ with the initial sputtering time, which
128 indicates the ultrathin 2D perovskite film was formed at the surface of 3D perovskite
129 layer. In the bulk (originally pure 3D) perovskite film, we now observe a relatively
130 uniform distribution of BA⁺ with an over 2-orders lower intensity compared with the
131 BA⁺ on the surface, indicating a clear diffusion process. Therefore, it is evident that
132 the bulk film contains both 3D and 2D perovskite with an increasing 2D concentration
133 towards the surface. Owing to the gradient distribution of BA⁺, the layer number (n)
134 of the 2D perovskites might increase from the surface to the bulk, creating a tendency
135 of bandgap narrowing (as illustrated in Fig. 1a and Supplementary Fig. 10b).

136 Grazing-incidence wide-angle X-ray scattering (GIWAXS) technique was carried
137 out to study the crystal orientation of the control and mixed DGFP perovskite films¹⁸.
138 The scattering patterns of perovskite films with various concentrations of BABr are
139 shown in Fig. 2a. The corresponding radial intensity profiles averaged over the whole
140 images are presented in Fig. 2b. The standard pure 3D perovskite film displays
141 uniform diffraction rings, indicating the formation of perovskite polycrystals with
142 randomly oriented cubic structure. For the perovskite films with the BABr
143 post-treatment, sharp diffraction peaks emerged at $q = 0.32, 0.64, \text{ and } 0.96 \text{ \AA}^{-1}$ along
144 the q_z direction (Fig. 2c), which are indexed as (020), (040), (060) planes of layered
145 2D perovskite crystals parallel to the substrate with a layer spacing of $\sim 20 \text{ \AA}$ ($n=2$)¹⁹.
146 The parallel 2D perovskite orientation is surprising, as it is commonly considered to
147 be unfavored for the overall vertical charge transport in solar cell devices. However,
148 the high efficiency PSC in this study indicates that the 2D perovskite layer with
149 relatively larger bandgap is thin enough for carrier transport, and can act as an
150 effective electron blocking layer to suppress the interfacial charge recombination. The
151 BABr GIWAXS peak appeared at $q_z = 0.41 \text{ \AA}^{-1}$ in the pure BABr film
152 (Supplementary Fig. 1a) and the excessive PbI_2 peak appeared at $q_z = 0.92 \text{ \AA}^{-1}$ in the
153 3D perovskite film were both absent, suggesting that 2D perovskite layers are
154 partially formed from the reaction of BABr with the excessive PbI_2 . When the
155 concentration of BABr increases, the 2D perovskite peaks become more intensive, as
156 the higher order (080) peak appears with the 5 mg/ml BABr treatment.

157 To provide more detailed evidence of the graded 2D perovskite from the surface
158 to the bulk, we conducted GIWAXS analysis at different X-ray incident angles to
159 elucidate the vertical structure of the surface and internal perovskite layers with
160 depth-dependent characterization as shown in Supplementary Fig. 2. The structure
161 information of perovskite film surface was recorded at a small incident angle of 0.1° ,
162 which shows the formation of 2D perovskite layer with $n=2$ only. When the angle of
163 incidence was increased to 0.3° , we can clearly observed some additional diffraction
164 peaks, which are assigned to be the (0k0) plane of 2D perovskite with $n=3$. With
165 increasing the incident angle and penetration depth, the diffraction peak intensity of

166 2D perovskite with $n=2, 3$ gradually increased. We can also clearly distinguish the
167 (222) plane of 2D perovskite with $n=2, 3$, and 4 at an incident angle of 1° . Thus, the
168 depth-dependent GIWAXS results are in good agreement with our hypothesis of
169 graded top 2D perovskite layers with increased n values for top-down distribution. To
170 further evaluate the structural property of the DGPF perovskite films, we performed
171 high-resolution transmission electron microscope (HRTEM) measurement with
172 focused ion beam (FIB) lift-out technique shown in Supplementary Fig. 3, which can
173 offer the chance to probe the crystal structure throughout the perovskite film. Here,
174 we selected two regions (region 1 and 2), which correspond to the top surface and
175 bulk, respectively. The region 1 (top surface) shows lattice fringes with characteristic
176 d-spacing of 13 \AA , which can be ascribed to 2D perovskite phases with $n=1$. At region
177 2 (bulk film), we can observe the characteristic d-spacing of 3D perovskite phase (3.2
178 \AA). Besides, it is worth noting that 2D perovskite phases with $n=2$ and 3 were
179 embedded within 3D perovskite phases, which may probably located at the grain
180 boundary.

181 The influence of the annealing time on the perovskite film was also investigated,
182 as shown in Supplementary Fig. 1. The 2D perovskite signals remain almost the same
183 for the samples with and without annealing, whereas, the 3D perovskite signals
184 become stronger with longer annealing time. The diffraction peaks shift towards
185 larger q values, indicating a slight lattice contraction²⁰. It is attributed to the
186 substitution of the relatively larger I^- ions with the smaller Br^- ions in 3D perovskite
187 crystals. The longer the annealing time, the more BABr diffused into the bulk film,
188 causing larger lattice contraction, consistent with the ToF-SIMS results. Therefore, as
189 illustrated in Fig. 2d, upon BABr post-treatment, BA^+ and Br^- ions tend to fill the
190 vacancies at grain boundaries of 3D perovskite due to the strong reactivity of
191 introduced BA^+ and Br^- ions with existed dangling bonds²¹. In this case, 2D
192 perovskite phases are most likely to form at the grain boundaries surrounding the 3D
193 perovskite phases. The 2D perovskite will heal and passivate the 3D perovskite
194 defects, significantly reduce the non-radiative recombination, which is in agreement
195 with the observed lower V_{OC} loss presented in the following.

196 Perovskite film morphology is another critical factor for photovoltaic
197 performance. Top-view scanning electron microscope (SEM) images and atomic force
198 microscopy (AFM) images of control and DGPF perovskite films are shown in Fig. 2e.
199 The morphology of the control RbCsMAFA perovskite film is uniform and compact
200 with well-crystallized grains, which is in good agreement with previous report ¹⁵.
201 With BABr treatment, an obvious grain coarsening process was observed, i.e., the
202 original small perovskite grains were merged into large ones via a thermodynamically
203 spontaneous Ostwald ripening process ²². We expected that the BABr molecules
204 would gradually penetrate into the existing 3D perovskite crystalline structure,
205 resulting in the formation of thin 2D perovskite phases on the top and the bulk of
206 mixed 2D/3D perovskites film. When a low concentration of BABr solution was used
207 (1 mg/ml or 2 mg/ml), we observe both large and small grains. It is reasonable to
208 expect that in the low concentration cases, the amount of BABr is not enough for
209 recrystallizing all the small-grain-sized 3D perovskite crystals. With further increase
210 of the BABr concentration to 5 mg/ml, the surface morphology became smoother with
211 uniformly distributed grain sizes.

212 The photovoltaic devices were fabricated using Spiro-OMeTAD as hole selective
213 layer (HSL) and Au as counter electrode. The current density–voltage (J – V) curves of
214 the champion control and DGPF PSCs are shown in Fig. 3a. The control
215 RbCsMAFA-based planar PSC device shows a decent champion PCE of 19.61% with
216 a short-circuit current density (J_{SC}) of 22.25 mA cm⁻², a V_{OC} of 1.161 V, and a fill
217 factor (FF) of 75.92%. The V_{OC} and J_{SC} are very close to EPFL reports on mesoporous
218 PSCs, while the FF is lower (0.76 vs. 0.81). After BABr treatment, the DGPF PSC
219 exhibits clear performance enhancement, yields a champion PCE of 20.24% when
220 using 1 mg/ml BABr, and 21.54% when using 2 mg/ml BABr, with an impressive V_{OC}
221 of 1.24 V (Supplementary Fig. 4). We fabricated 20 devices in each condition, and the
222 detailed statistical analysis is summarized in Supplementary Table 4. The statistics of
223 two types of devices (control and DGPF PSCs @2 mg/ml BABr) is shown in
224 Supplementary Fig. 5, which indicates good reproducibility in DGPF PSCs with an
225 improved PCE of 20.38% ($\pm 0.38\%$) on average compares to 18.80% ($\pm 0.31\%$) in

226 control PSCs. A much enhanced average V_{OC} of 1.22 V ($\pm 0.02V$) in the DGPF PSC,
 227 compares to 1.15 V ($\pm 0.02V$) in pure 3D PSCs, is the major factor contributing to the
 228 overall efficiency enhancement. Considering the almost same optical bandgap for the
 229 control and DGPF perovskite films, the driving force of high V_{OC} values with a small
 230 W_{OC} for the DGPF PSCs are of great interest.

231 The external quantum efficiency (EQE) data of PSCs with different BABr
 232 conditions are shown in Supplementary Fig. 4b. As expected, the EQE spectrum is
 233 softly blue-shifted when incorporating BABr, which is very small and do not lead to
 234 the J_{SC} reduction. We observed better photo response in the long wavelength range for
 235 the devices treated with BABr solutions, which may originate from enhanced charge
 236 transports²³. For the RbCsMAFA system, when using the BABr solution with an
 237 optimized concentration of 2 mg/ml, the 21.54% PCE cell achieved is also
 238 hysteresis-free, and the stabilized PCE is 21.27%, as shown in Fig. 3a and
 239 Supplementary Fig. 6. Here, we also compared some results of PSCs with over 21%
 240 PCE, where the W_{OC} varies from 0.39 to 0.48 V, and our DGPF device demonstrated a
 241 record V_{OC} among them (Supplementary Fig. 7 and Table 3)^{15,24}.

242 To understand the fundamental of the high V_{OC} in these PSCs in a quantitative
 243 manner, the accurate determination of perovskite bandgap is critical. As shown in
 244 Supplementary Fig. 8, the determination of optical bandgaps was conducted in two
 245 widely recognized methods: (a) Using the maximum point of the derivative of the
 246 EQE spectra (i.e. $dEQE/dE$)²⁵, and (b) Tauc plot method)²⁶. The E_g values from the
 247 two methods agree very well.

248 We first exam the electroluminescence (EL) efficiency. The reciprocity relation
 249 can describe the relationship between the photovoltaic quantum efficiency (EQE_{PV})
 250 and the external quantum efficiency of the electroluminescence (EQE_{EL}), which can
 251 be used to quantify the V_{OC} loss in photovoltaic devices²⁷. According to Rau,
 252 $\Phi_{EL}(E) = \varphi_{BB}(E)EQE_{PV}(E) \left[\exp\left(\frac{qV}{kT}\right) - 1 \right]$, where $\varphi_{BB}(E)$ is the black body
 253 emission flux density, the $\Phi_{EL}(E)$ is the EL spectral photon flux ($\Phi_{EL}(E) =$
 254 $\frac{J_{inj}(V)}{q}EQE_{EL}(E)$), and $J_{inj}(V)$ is the injected current. As shown in Fig. 3b, the

255 extracted EQE_{PV} exhibited a nearly exact dependence on energy as the measured
 256 EQE_{PV} , implying the reciprocity relations hold. Herein, we identify the origins of
 257 increased open-circuit voltage in DGPF PSCs by quantifying the dominating
 258 recombination mechanisms. The first term $V_{\text{OC},\text{rad}}$ describes the radiative limit of
 259 V_{OC} , which is determined by $V_{\text{OC},\text{rad}} = \frac{kT}{q} \ln \left[\frac{J_{\text{SC}}}{\int_0^\infty \text{EQE}_{\text{PV}}(E) \phi_{\text{BB}}(E) dE} + 1 \right]^6$. The
 260 calculated $V_{\text{OC},\text{rad}}$ is 1.35 V for both reference control and DGPF perovskite devices,
 261 both with almost the same 1.63 eV bandgap²⁸. Therefore, the difference in the
 262 non-radiative recombination losses is the source of V_{OC} enhancement. We then
 263 quantify the second term non-radiative recombination voltage loss ($\Delta V_{\text{OC},\text{nr}}$), which in
 264 principle can be estimated from the measured EQE_{EL} , with the relationship of
 265 $\Delta V_{\text{OC},\text{nr}} = V_{\text{OC},\text{rad}} - V_{\text{OC}} = -\frac{kT}{q} \ln \text{EQE}_{\text{EL}}$. An EQE_{EL} of 0.85% was measured for a
 266 DGPF PSC device under LED mode with forward bias current density of 22.22
 267 mA/cm^2 (Fig. 3c). This external EL quantum efficiency is very close that of the most
 268 efficient silicon solar cell ($\sim 0.5\%$)²⁹. This is also one of the highest values obtained in
 269 PSCs. The 0.85% EQE_{EL} corresponds to a $\Delta V_{\text{OC},\text{nr}}$ of 0.12 V^{15,30}, which agree well
 270 with the device parameter ($V_{\text{OC}} = 1.23$ V for the tested device). For the champion
 271 efficiency device with a V_{OC} of 1.24 V, the EQE_{EL} should be higher, and the $\Delta V_{\text{OC},\text{nr}}$
 272 will be 0.11 V. The maximum V_{OC} of 1.25 V with 20.15% PCE for the DGPF PSC
 273 device indicates a 100 mV $\Delta V_{\text{OC},\text{nr}}$ (Supplementary Fig. 9). On the other hand, the
 274 control PSC has a V_{OC} of 1.16 V. Under the forward bias LED mode with the same
 275 injected current density of 22.22 mA/cm^2 , the PSC delivers an EQE_{EL} of 0.065%
 276 (corresponding to $\Delta V_{\text{OC},\text{nr}}$ of 0.19 V from the equation), which also agrees well with
 277 the device V_{OC} loss analysis. The extraordinarily low non-radiative recombination
 278 losses in DGPF PSCs are the dominating reason behind the high V_{OC} as well as the
 279 high efficiencies in these PSC devices. Generally, these non-radiative recombination
 280 losses arise from defects (charge carrier traps) either in the bulk photovoltaic
 281 materials or at the interfaces.

282 The ultraviolet photoelectron spectroscopy (UPS) on 3D perovskite films with
 283 different BA₂Br concentrations are performed to understand electronic properties of

284 the films. Supplementary Fig. 10a shows the cutoff energy (E_{cutoff}) in high binding
285 energy region and valence band (VB) with respect to vacuum level derived from UPS
286 spectra. With the increase of BABr concentration, the E_{cutoff} shifts to higher binding
287 energy, indicating the ion-exchange induced 3D to 2D phase transition can reduce the
288 Fermi level of RbCsMAFA¹⁹. The valence band edges determined by the linear
289 portion in low binding energy region for 0-BABr, 1-BABr, 2-BABr, and 5-BABr are
290 located at 5.86, 5.80, 5.74, and, 5.70 eV, respectively. Here, to mimic a similar
291 situation, a thinner ~100 nm 3D perovskite films with and without BABr treatment
292 are used to enhance signal-noise-ratio. The absorption spectra of the thin control and
293 DGPF perovskite films are shown in Supplementary Fig. 11. It is noteworthy that the
294 absorption peak could be observed at 2.27, 2.05, and 1.81 eV, which are assigned to
295 2D perovskites with $n=2$, 3, and 4, respectively. As discussed above, the
296 depth-dependent GIWAXS data also confirmed this graded distribution. The top-down
297 structure information shows that the 2D perovskites with small n value ($n=2$) are
298 prone to be existed near the surface. Due to graded distribution of BA^+ in the 2D
299 perovskite region (Figure 1c), the energy diagram at the perovskite/HTL interface can
300 be estimated³¹. As shown in Supplementary Fig. 10b, the energy diagram of
301 perovskites with gradient energy structure distribution for the 2mg/ml BABr treated
302 case is depicted. Compare to pure 3D perovskite device, the graded 2D perovskites
303 lead to a graded energy level transition from bulk 3D perovskite to 2D perovskite. The
304 energy level shift is not linear, envisioned from BA^+ spatial distribution. We can
305 expect the energy level gradient is smooth close to bulk perovskite, but the gradient is
306 much faster when reaching the spiro-OMeTAD HTL side. Therefore, the
307 aforementioned graded 2D perovskite layer can be regarded as of the same function as
308 the graded window layer in traditional thin film solar cells, which provide a potential
309 barrier for the electrons³². The electrons moving towards perovskite top surface
310 (where the trap state density is higher than that in the bulk) will be reflected back
311 close to the interface. This energy level alignment thus will further eliminate the
312 surface recombination effectively. In the meantime, the mildly graded valence band
313 energy level alignment transition can also facilitate efficient hole transport from

314 perovskite to HTM.

315 Photoluminescence (PL) and time-resolved PL (TRPL) measurements were
316 conducted for the various perovskite films to examine the defect passivation effect
317 (Supplementary Fig. 12). For the DGPF perovskite films, in addition to a significant
318 PL intensity enhancement, we observed a slight blue-shift of the PL peaks, which
319 agree with the scenario of the Br⁻ substitution to I⁻, and the resulted shrinkage of the
320 3D crystal lattice. The carrier lifetime of control perovskite film was significantly
321 increased in the self-passivated DGPF perovskite films. All DGPF perovskite films
322 exhibit a long exponential PL decay tail with PL lifetimes above 1 μ s (in particular, a
323 PL lifetime of 1.86 μ s was obtained for 2-BABr sample), contrasting the shorter one
324 (0.76 μ s) for the control perovskite film. This is consistent with the higher voltages
325 shown in Fig. 3c for DGPF perovskite devices, in which the defects were effectively
326 passivated³³. Furthermore, we measure the external photoluminescence quantum
327 efficiency (PLQE) for the perovskite films with different contacts. The geometry of
328 the PL measurement is shown in Supplementary Fig. 13, in which the light excitation
329 either from top side or bottom sides. Here we used an incident laser with wavelength
330 of 485 nm, which has a penetration depth less than 100 nm according to Snell's law,
331 which implies that we can mainly collect the PL signal near the top surface of
332 perovskite film under the front excitation³⁴. The PLQE of DGPF perovskite film
333 deposited on the glass reaches a value of 13.58%, whereas only 4.65% for control
334 perovskite film. When the presence of charge selective contacts (electrons or holes),
335 the PLQE values for both control and DGPF perovskite films decrease, which can be
336 ascribed to the quench effect and introduced non-radiative channels at the contact
337 interface³⁵. We again observe that the DGPF approach enable a less notable reduction
338 in PLQE upon presence of selective contacts. In the case of light excitation from
339 either top or bottom, the higher PLQEs for the DGPF perovskite samples suggest that
340 optoelectronic properties of perovskite film as well as its related interfaces and
341 surfaces can be optimized via DGPF method.

342 Highly sensitive photothermal deflection spectroscopy (PDS) technique is
343 conducted to study the sub bandgap/trap state absorption and energetic disorder in

344 these samples ³⁶. A decrease of sub-bandgap absorption determined by the PDS is
345 clearly seen in the DGPF perovskite films, indicating reduced sub-bandgap states
346 (trap states). The presence of electronic sub-bandgap trap states is one of the origins
347 of non-radiative recombination pathways ^{37,38}. The internal passivation derived from
348 2D perovskite participation in the final DGPF perovskite film can effectively suppress
349 non-radiative recombination to incur minimal voltage losses. PDS result comes with a
350 characteristic Urbach energy. The Urbach energies, estimated from the PDS spectra
351 are 20.55, 19.7, 19.9, and 23.21 meV for the sample treated with the BABr
352 concentration of 0 mg/ml, 1 mg/ml, 2 mg/ml, and 5 mg/ml, respectively
353 (Supplementary Fig. 14). The lower Urbach energy indicates a lower level of
354 electronic disorder in the perovskite films with a low concentration of BABr treatment,
355 which agrees with the enhancement of V_{OC} ³⁹. When increasing the BABr
356 concentrations to 5 mg/ml, we observe a gentle band-edge absorption rise, indicating
357 increased energy disorder. As the inherent Urbach energy in 2D perovskite is higher
358 compared to 3D counterparts, this is expected and also consistent with the decreasing
359 device performance when treating with higher concentration of BABr. The PDS result
360 of 2D perovskites is shown in Supplementary Fig. 15, which shows the Urbach
361 energy of 2D perovskite is 38.4 meV.

362 We further performed electronic structure calculations based on density
363 functional theory (DFT) calculations to investigate the passivation mechanism at
364 BA/perovskite interface. The surface terminated with (110) plane was used for the
365 calculations. Charge density calculations based on the DFT were performed to
366 characterize how amine, including BA molecule, can passivate the
367 $CS_{0.125}FA_{0.875}Pb(I_{0.85}Br_{0.15})_3$ surfaces. The anti-site defect is modeled, such as Pb_{Br} or
368 Pb_I , known as deep-level defects and the most detrimental defects in perovskite solar
369 cells⁴⁰. As illustrated in Supplementary Fig. 16, the charge distribution is localized
370 around the anti-site defect site, which can produce the recombination center and
371 capture the carriers. After interaction with BA molecule, we first find that the nitrogen
372 (N) will bond with Pb atoms and then the previous anti-site defect can be passivated,
373 shown in Supplementary Fig. 16c, like the perfect surface without defect indicating by

374 Supplementary Fig. 16b. Without the dopant BA, the localized electron distribution is
375 observed clearly in Supplementary Fig. 16a. The adsorption of BA will make the
376 charge distribution delocalized, indicating that the trap states caused by anti-site
377 defect are passivated. Trap density of states (tDOS) of control and DGPF devices are
378 further examined, showing a much lower tDOS in DGPF devices, which is consistent
379 with DFT calculation (Supplementary Fig. 17).

380 The effectiveness of the DGPF approach has validated in more perovskite
381 systems. In double cation $\text{MA}_{0.7}\text{FA}_{0.3}\text{PbI}_3$ perovskite system, XRD measurement was
382 conducted to analysis the crystal structure of the formed DGPF perovskite film
383 (Supplementary Fig. 18). The perovskite film shows slight peak shift towards higher
384 2θ degrees, which is consistent with the findings from quaternary RbCsMAFA
385 perovskite system. The GIWAXS results in Supplementary Fig. 19 clearly show the
386 2D diffractive peaks for the BABr -treated samples. The formed 2D perovskite top
387 layer consists of layered 2D perovskites with different n values ($n=2$ & $n=3$). The
388 device performance based on these narrower-bandgap perovskite ($\text{MA}_{0.7}\text{FA}_{0.3}\text{PbI}_3$,
389 $E_g=1.55$ eV) are shown in Supplementary Fig. 20. The best-performing
390 $\text{MA}_{0.7}\text{FA}_{0.3}\text{PbI}_3$ PSC with 2 mg/ml BABr post-treatment ($E_g=1.56$ eV) exhibits a V_{OC}
391 of 1.161 V, a J_{SC} of 22.95 mA/cm^2 , and a FF of 77.67%, featuring a high PCE of
392 20.67%. For comparison, the control pure 3D device has a lower PCE of 18.59%. The
393 significantly enhanced V_{OC} for the DGPF PSCs is associated with a significantly
394 reduced V_{OC} deficit, i.e., W_{OC} of 0.40V.

395 This method was also tested in wide-bandgap (WBG) mixed-cation Pb PSCs,
396 which has the significance of being potentially an ideal WBG subcell for tandem
397 perovskite PSCs towards higher efficiency^{41, 42}. By means of DGPF approach, the
398 best-performing wide-bandgap $\text{FA}_{0.8}\text{Cs}_{0.2}\text{Pb}(\text{I}_{0.7}\text{Br}_{0.3})_3$ PSC ($E_g=1.73$ eV) has a PCE of
399 18.09% with a W_{OC} of 0.48 V and an outstanding V_{OC} of 1.26 V (Supplementary Fig.
400 21)⁴³. This is again one of the highest V_{OC} , and lowest W_{OC} in ~ 1.73 eV bandgap
401 PSCs, to our knowledge⁴⁴. Hysteresis analysis of representative PSCs based on
402 various optical bandgaps is shown in Supplementary Fig. 22 and summarized in
403 Supplementary Table 4. Devices after incorporating BABr exhibit lower J - V

404 hysteresis compared to the control pure 3D PSC device, which is consistent with the
405 scenario that larger BA moieties mitigate or even prohibit ion migration and reduce
406 defect mentioned above. The data of voltage loss analysis in perovskite devices with
407 different bandgaps were summarized in Table 1.

408 We further proved the effectiveness of DGPF approach in a ~ 1.53 eV perovskite
409 system ($\text{Cs}_{0.03}(\text{FA}_{0.97}\text{MA}_{0.03})_{0.97}\text{Pb}(\text{I}_{0.97}\text{Br}_{0.03})_3$) with a modified SnO_2 QDs ETL. A
410 champion PCE up to 23.78% (average PCE: $23.24 \pm 0.33\%$, certified PCE: 23.09%,
411 Figure S27) with a maximum V_{OC} of 1.210 V (W_{OC} as low as 0.326 V) was achieved,
412 as shown in Fig. 3d. The bandgap of perovskite was calculated through the
413 combination of EQE and UV-vis absorption spectra (see Supplementary Fig. 23, 24).
414 More details can be found in Supplementary Fig. 25-27 and Supplementary Table 7.
415 To evaluate the $\Delta V_{\text{OC,nr}}$, we measured the EQE_{EL} for a complete PSC device operating
416 as a LED in forward voltage bias, as shown in Fig. 3f. The DGPF device exhibited an
417 EQE_{EL} up to 5.78% at an injection current equal to J_{SC} (24.57 mA/cm^2),
418 corresponding to a $\Delta V_{\text{OC,nr}}$ of 74 mV, which agreed well with the estimated value from
419 W_{OC} . To the best of our knowledge, 0.326 V W_{OC} is among the lowest in all reported
420 perovskite systems.

421 In addition to device performance, the operational stability of PSCs is also vital
422 for PSC technology. We first investigated the long-term stability of control and DGPF
423 PSCs (non-encapsulated) under dark storage in the ambient conditions with 30%
424 relative humidity (RH) (Supplementary Fig. 28). The DGPF PSCs showed
425 significantly enhanced resistivity to humidity, virtually no PCE degradation after 45
426 days. This is attributed to the improved hydrophobicity of perovskite structure after
427 introducing large organic cation (BA). We further studied the stability of encapsulated
428 device under continues simulated sunlight illumination (~ 35 °C) at open-circuit
429 condition. The DGPF PSCs showed much slower performance degradation compared
430 to pure 3D PSCs. The encapsulated DGPF PSCs retained 62% of the initial PCE after
431 800 h illumination, while the control 3D PSCs only retain the 25% of the original
432 PCE under the same conditions (Fig. 4). All the device parameters recorded during the
433 stability test (Supplementary Fig. 29a and b), are shown in Supplementary Table 5 and

434 6. ‘Burn-in’ exponential degradation regime was clearly observed in both types of
435 devices, which is a common phenomenon for PSCs and organic solar cells^{25, 45, 46}.
436 More specifically, both types of PSCs experienced a faster performance degradation
437 process (around 100 h), followed by a slower steady degradation. For the
438 encapsulated DGPF PSCs, the T_{80} (i.e. lose 20% initial PCE) post burn-in lifetime is
439 700 h under 0.8-sun illumination. However, the T_{80} post burn-in lifetime for pure 3D
440 PSC devices are significantly shorter at ~ 300 h. To exclude the effects of interface
441 layers (particularly the spiro-OMeTAD HTM) and electric load (under maximum
442 power point (MPP) or OC) on the device operational stability, we fabricated
443 perovskite devices with a planar p-i-n structure (Supplementary Fig. 30a and b) and
444 performed long-term stability test of encapsulated devices illuminated under
445 continuous 1-sun irradiation by LED lamp at a temperature of ~ 60 °C in air condition
446 as shown in Fig. 4b⁴⁵. At MPP condition, we found that both control and DGPF
447 devices showed obviously decreased degradation rates compared that at OC, which
448 can be ascribed to role of excess charge carrier. Finally, our DGPF devices can retain
449 91% of initial efficiency after 516 h of continuous illumination operation in ambient
450 air conditions. In comparison, the control device only retained 16% of the original
451 PCE under the same conditions.

452 In summary, we developed a simple DGPF self-passivation strategy for high
453 performance PSCs, which simultaneously achieved both bulk and interface 2D
454 perovskite passivation of the PSCs. The DGPF strategy dramatically boost the PCE of
455 1.63 eV quaternary-cation PSCs to 21.54%, with a superb V_{OC} of 1.24 V; we further
456 improved the PCE up to 23.78% (certified 23.09%) with the maximum V_{OC} of 1.21 V
457 in a ~ 1.53 eV perovskite system, i.e. W_{OC} as low as 0.326 V. Non-radiative
458 recombination losses in perovskite materials and devices can be reduced to as low as
459 74 mV (from EQE_{EL} measurement), one of the lowest reported to date. The method is
460 universally applicable to PSCs of different bandgaps. Moreover, significantly
461 enhanced operation stability is achieved with the simultaneous 2D perovskite
462 passivation in bulk and interfaces. The DGPF approach paves the way to further
463 approach the theoretical PSC efficiency limit via the elimination of non-radiative

464 recombination decay, and is a step forward to achieve highly efficient PSCs with
465 long-term operational stability.

466

467

468

469

470

471

472

473

474 References

- 475 1. Jeon NJ, Na H, Jung EH, Yang T-Y, Lee YG, Kim G, *et al.* A fluorene-terminated
476 hole-transporting material for highly efficient and stable perovskite solar cells. *Nature Energy*
477 2018.
- 478 2. Green M, Dunlop E, Hohl - Ebinger J, Yoshita M, Kopidakis N, Hao X. Solar cell efficiency
479 tables (version 57). *Progress in Photovoltaics: Research and Applications* 2020, 29(1): 3-15.
- 480 3. Hardin BE, Snaith HJ, McGehee MD. The renaissance of dye-sensitized solar cells. *Nature*
481 *Photonics* 2012, 6(3): 162-169.
- 482 4. Tress W, Marinova N, Inganäs O, Nazeeruddin MK, Zakeeruddin SM, Graetzel M. Predicting
483 the Open-Circuit Voltage of CH₃NH₃PbI₃ Perovskite Solar Cells Using Electroluminescence
484 and Photovoltaic Quantum Efficiency Spectra: the Role of Radiative and Non-Radiative
485 Recombination. *Advanced Energy Materials* 2015, 5(3): 1400812.
- 486 5. Yin W-J, Yang J-H, Kang J, Yan Y, Wei S-H. Halide perovskite materials for solar cells: a
487 theoretical review. *Journal of Materials Chemistry A* 2015, 3(17): 8926-8942.
- 488 6. Yao J, Kirchartz T, Vezie MS, Faist MA, Gong W, He Z, *et al.* Quantifying Losses in Open-Circuit
489 Voltage in Solution-Processable Solar Cells. *Physical Review Applied* 2015, 4(1).
- 490 7. Luo D, Yang W, Wang Z, Sadhanala A, Hu Q, Su R, *et al.* Enhanced photovoltage for inverted
491 planar heterojunction perovskite solar cells. *Science* 2018, 360(6396): 1442-1446.
- 492 8. Zheng D, Peng R, Wang G, Logsdon JL, Wang B, Hu X, *et al.* Simultaneous Bottom-Up
493 Interfacial and Bulk Defect Passivation in Highly Efficient Planar Perovskite Solar Cells using
494 Nonconjugated Small-Molecule Electrolytes. *Advanced materials* 2019, 31(40): e1903239.
- 495 9. Motti SG, Meggiolaro D, Martani S, Sorrentino R, Barker AJ, De Angelis F, *et al.* Defect Activity
496 in Metal-Halide Perovskites. *Advanced materials* 2019: e1901183.
- 497 10. Yang G, Wang C, Lei H, Zheng X, Qin P, Xiong L, *et al.* Interface engineering in planar
498 perovskite solar cells: energy level alignment, perovskite morphology control and high
499 performance achievement. *Journal of Materials Chemistry A* 2017, 5(4): 1658-1666.
- 500 11. Kim M, Kim G-H, Lee TK, Choi IW, Choi HW, Jo Y, *et al.* Methylammonium Chloride Induces
501 Intermediate Phase Stabilization for Efficient Perovskite Solar Cells. *Joule* 2019, 3(9):
502 2179-2192.
- 503 12. Yin W-J, Shi T, Yan Y. Unusual defect physics in CH₃NH₃PbI₃ perovskite solar cell absorber.
504 *Applied Physics Letters* 2014, 104(6): 063903.
- 505 13. Stolterfoht M, Caprioglio P, Wolff CM, Márquez JA, Nordmann J, Zhang S, *et al.* The impact of
506 energy alignment and interfacial recombination on the internal and external open-circuit
507 voltage of perovskite solar cells. *Energy & Environmental Science* 2019, 12(9): 2778-2788.
- 508 14. Yang G, Chen C, Yao F, Chen Z, Zhang Q, Zheng X, *et al.* Effective Carrier-Concentration Tuning
509 of SnO₂ Quantum Dot Electron-Selective Layers for High-Performance Planar Perovskite Solar
510 Cells. *Advanced materials* 2018.
- 511 15. Saliba M, Matsui T, Domanski K, Seo J-Y, Ummadisingu A, Zakeeruddin SM, *et al.*
512 Incorporation of rubidium cations into perovskite solar cells improves photovoltaic
513 performance. *Science* 2016, 354(6309): 206-209.
- 514 16. Yadav P, Dar MI, Arora N, Alharbi EA, Giordano F, Zakeeruddin SM, *et al.* The Role of Rubidium
515 in Multiple-Cation-Based High-Efficiency Perovskite Solar Cells. *Advanced materials* 2017,
516 29(40).

- 517 17. Albadri A, Yadav P, Alotaibi M, Arora N, Alyamani A, Albrithen H, *et al.* Unraveling the Impact
518 of Rubidium Incorporation on the Transport-Recombination Mechanisms in Highly Efficient
519 Perovskite Solar Cells by Small-Perturbation Techniques. *The Journal of Physical Chemistry C*
520 2017, **121**(45): 24903-24908.
- 521 18. Shao S, Liu J, Portale G, Fang H-H, Blake GR, ten Brink GH, *et al.* Highly Reproducible Sn-Based
522 Hybrid Perovskite Solar Cells with 9% Efficiency. *Advanced Energy Materials* 2018, **8**(4):
523 1702019.
- 524 19. Cao DH, Stoumpos CC, Farha OK, Hupp JT, Kanatzidis MG. 2D Homologous Perovskites as
525 Light-Absorbing Materials for Solar Cell Applications. *Journal of the American Chemical*
526 *Society* 2015, **137**(24): 7843-7850.
- 527 20. Lee J-W, Kim D-H, Kim H-S, Seo S-W, Cho SM, Park N-G. Formamidinium and Cesium
528 Hybridization for Photo- and Moisture-Stable Perovskite Solar Cell. *Advanced Energy*
529 *Materials* 2015, **5**(20): 1501310.
- 530 21. Zhang T, Long M, Yan K, Qin M, Lu X, Zeng X, *et al.* Crystallinity Preservation and Ion Migration
531 Suppression through Dual Ion Exchange Strategy for Stable Mixed Perovskite Solar Cells.
532 *Advanced Energy Materials* 2017, **7**(15): 1700118.
- 533 22. Baldan A. Review progress in Ostwald ripening theories and their applications to nickel-base
534 superalloys Part I: Ostwald ripening theories. *Journal of materials science* 2002, **37**(11):
535 2171-2202.
- 536 23. Yang G, Qin P, Fang G, Li G. A Lewis Base - Assisted Passivation Strategy Towards Highly
537 Efficient and Stable Perovskite Solar Cells. *Solar RRL*: 1800055.
- 538 24. Abdi-Jalebi M, Andaji-Garmaroudi Z, Cacovich S, Stavrakas C, Philippe B, Richter JM, *et al.*
539 Maximizing and stabilizing luminescence from halide perovskites with potassium passivation.
540 *Nature* 2018, **555**(7697): 497-501.
- 541 25. Wang Z, Lin Q, Chmiel FP, Sakai N, Herz LM, Snaith HJ. Efficient ambient-air-stable solar cells
542 with 2D–3D heterostructured butylammonium-caesium-formamidinium lead halide
543 perovskites. *Nature Energy* 2017, **2**(9): 17135.
- 544 26. Eperon GE, Stranks SD, Menelaou C, Johnston MB, Herz LM, Snaith HJ. Formamidinium lead
545 trihalide: a broadly tunable perovskite for efficient planar heterojunction solar cells. *Energy &*
546 *Environmental Science* 2014, **7**(3): 982.
- 547 27. Rau U. Reciprocity relation between photovoltaic quantum efficiency and electroluminescent
548 emission of solar cells. *Physical Review B* 2007, **76**(8).
- 549 28. Tress W, Yavari M, Domanski K, Yadav P, Niesen B, Correa Baena JP, *et al.* Interpretation and
550 evolution of open-circuit voltage, recombination, ideality factor and subgap defect states
551 during reversible light-soaking and irreversible degradation of perovskite solar cells. *Energy &*
552 *Environmental Science* 2018, **11**(1): 151-165.
- 553 29. Green MA. Radiative efficiency of state - of - the - art photovoltaic cells. *Progress in*
554 *Photovoltaics: Research and Applications* 2012, **20**(4): 472-476.
- 555 30. Bi D, Tress W, Dar MI, Gao P, Luo J, Renevier C, *et al.* Efficient luminescent solar cells based on
556 tailored mixed-cation perovskites. *Science advances* 2016, **2**(1): e1501170.
- 557 31. Liu J, Leng J, Wu K, Zhang J, Jin S. Observation of Internal Photoinduced Electron and Hole
558 Separation in Hybrid Two-Dimensional Perovskite Films. *Journal of the American Chemical*
559 *Society* 2017, **139**(4): 1432-1435.
- 560 32. Nelson J. *The physics of solar cells*. World Scientific Publishing Company, 2003.

- 561 33. Turren-Cruz S-H, Saliba M, Mayer MT, Juárez-Santiesteban H, Mathew X, Nienhaus L, *et al.*
562 Enhanced charge carrier mobility and lifetime suppress hysteresis and improve efficiency in
563 planar perovskite solar cells. *Energy & Environmental Science* 2018, **11**(1): 78-86.
- 564 34. Lin Y, Fang Y, Zhao J, Shao Y, Stuard SJ, Nahid MM, *et al.* Unveiling the operation mechanism
565 of layered perovskite solar cells. *Nature communications* 2019, **10**(1): 1008.
- 566 35. Sarritzu V, Sestu N, Marongiu D, Chang X, Masi S, Rizzo A, *et al.* Optical determination of
567 Shockley-Read-Hall and interface recombination currents in hybrid perovskites. *Scientific*
568 *reports* 2017, **7**: 44629.
- 569 36. Jackson WB, Amer NM, Boccarda A, Fournier D. Photothermal deflection spectroscopy and
570 detection. *Applied optics* 1981, **20**(8): 1333-1344.
- 571 37. Stranks SD, Burlakov VM, Leijtens T, Ball JM, Goriely A, Snaith HJ. Recombination Kinetics in
572 Organic-Inorganic Perovskites: Excitons, Free Charge, and Subgap States. *Physical Review*
573 *Applied* 2014, **2**(3).
- 574 38. Stranks SD. Nonradiative Losses in Metal Halide Perovskites. *ACS Energy Letters* 2017, **2**(7):
575 1515-1525.
- 576 39. Shao Y, Yuan Y, Huang J. Correlation of energy disorder and open-circuit voltage in hybrid
577 perovskite solar cells. *Nature Energy* 2016, **1**(1): 15001.
- 578 40. Chen B, Rudd PN, Yang S, Yuan Y, Huang J. Imperfections and their passivation in halide
579 perovskite solar cells. *Chemical Society reviews* 2019.
- 580 41. McMeekin DP, Sadoughi G, Rehman W, Eperon GE, Saliba M, Hörantner MT, *et al.* A
581 mixed-cation lead mixed-halide perovskite absorber for tandem solar cells. *Science* 2016,
582 **351**(6269): 151-155.
- 583 42. Zhao D, Wang C, Song Z, Yu Y, Chen C, Zhao X, *et al.* Four-Terminal All-Perovskite Tandem
584 Solar Cells Achieving Power Conversion Efficiencies Exceeding 23%. *ACS Energy Letters* 2018,
585 **3**(2): 305-306.
- 586 43. Yu Y, Wang C, Grice CR, Shrestha N, Zhao D, Liao W, *et al.* Synergistic Effects of Lead
587 Thiocyanate Additive and Solvent Annealing on the Performance of Wide-Bandgap Perovskite
588 Solar Cells. *ACS Energy Letters* 2017, **2**(5): 1177-1182.
- 589 44. Zhou Y, Wang F, Cao Y, Wang J-P, Fang H-H, Loi MA, *et al.* Benzylamine-Treated Wide-Bandgap
590 Perovskite with High Thermal-Photostability and Photovoltaic Performance. *Advanced Energy*
591 *Materials* 2017, **7**(22): 1701048.
- 592 45. Domanski K, Alharbi EA, Hagfeldt A, Grätzel M, Tress W. Systematic investigation of the
593 impact of operation conditions on the degradation behaviour of perovskite solar cells. *Nature*
594 *Energy* 2018, **3**(1): 61-67.
- 595 46. Kong J, Song S, Yoo M, Lee GY, Kwon O, Park JK, *et al.* Long-term stable polymer solar cells
596 with significantly reduced burn-in loss. *Nature communications* 2014, **5**: 5688.
- 597 47. Chen B, Song J, Dai X, Liu Y, Rudd PN, Hong X, *et al.* Synergistic Effect of Elevated Device
598 Temperature and Excess Charge Carriers on the Rapid Light-Induced Degradation of
599 Perovskite Solar Cells. *Advanced materials* 2019, **31**(35): e1902413.
- 600 48. Lin Y, Chen B, Fang Y, Zhao J, Bao C, Yu Z, *et al.* Excess charge-carrier induced instability of
601 hybrid perovskites. *Nature communications* 2018, **9**(1): 4981.
- 602
603
604

605

606

607 **Data availability**

608 The data that support the plots within this paper and other findings of this study are
609 available from the corresponding author upon reasonable request

610

611 **Acknowledgements**

612 G.L. would like to thank the support by Research Grants Council of Hong Kong
613 (Grant No. C5037-18G, 15246816, and 15218517), Shenzhen Science and
614 Technology Innovation Commission (Project No. JCYJ20170413154602102), and the
615 funding provided by the Hong Kong Polytechnic University (Project Code: 1-ZE29,
616 1-BBAS, and Sir Sze-yuen Chung Endowed Professorship Fund (8-8480)). G.F.
617 acknowledges the support of National High Technology Research and Development
618 Program (No. 2015AA050601), the National Natural Science Foundation of China
619 (Nos. 11674252 and 62074117) and the Natural Science Foundation of Hubei
620 Province (No. 2019AAA020). X.L. and M.Q. acknowledge the financial support from
621 Research Grant Council of Hong Kong (General Research Fund No. 14314216)

622

623 **Author contributions**

624 G.L., G.Y. and Y.Y. proposed the idea and designed the experiment. G.Y. and Z.R.
625 fabricated and characterized perovskite solar cells. Z.R., K.L. and Q.L. prepared and
626 characterized the devices for the efficiency certification of PSCs. G.Y. conducted
627 SEM, AFM, XRD, and PL measurements. X.L. and M.Q. carried out GIWAXS
628 measurement and analyzed the results. W.D. and H.W. conducted the EL measurement
629 and discussed the radiative and non-radiative recombination loss analysis. Y.C.
630 performed DFT calculations on the BA molecule passivation under the supervision of
631 T.S. and X.W. B.G. and J.H. helped to measure the Ultrasensitive EQE. D.L. and S.L.
632 contributed to the PLQY measurement. J.L., H.W., and F.Y. carried out the UPS and
633 absorption measurements. H.Y. and S.K.S contributed to the photothermal deflection
634 spectroscopy data. H.Z. contributed to the ToF-SIMS result analysis. Y.Z performed
635 the HRTEM measurement and analyzed the results under the supervision of J.W.. G.L.,
636 G.F., Y.Y., G.Y., Z.R., K.L., and X.L. prepared, revised, and finalized the manuscript.
637 All the authors discussed the results and commented on the manuscript.

638

639 **Competing financial interests**

640 The authors declare no competing financial interests.

641

642 **Methods**

643 **Materials and Methods**

644 Preparation of RbCsMAFA ($\text{Rb}_{0.05}\text{Cs}_{0.05}[(\text{FA}_{0.83}\text{MA}_{0.17})]_{0.9}\text{Pb}(\text{I}_{0.83}\text{Br}_{0.17})_3$)

645 First, a nonstoichiometric precursor solution for $(\text{FA}_{0.83}\text{MA}_{0.17})\text{Pb}(\text{I}_{0.83}\text{Br}_{0.17})_3$
646 was prepared by dissolving 1.1 M PbI_2 (TCI), 1 M FAI (Dyesol), 0.22 M PbBr_2 , and

647 0.2 M MABr (Dyesol) in 1 mL of a 4 : 1 (v/v) mixture of anhydrous DMF and DMSO.
648 (Please note the volume changes upon dissolving these salts) 40 μ L of 1.5 M CsI
649 (Alfa Aesar) pre-dissolved in 1mL DMSO and 40 μ L of 1.5 M RbI (Alfa Aesar)
650 pre-dissolved in 1mL of a 4 : 1 (v/v) mixture of anhydrous DMF and DMSO were
651 then added to the as-prepared $(\text{FA}_{0.83}\text{MA}_{0.17})\text{Pb}(\text{I}_{0.83}\text{Br}_{0.17})_3$ solution, yielding a
652 quadruple cation perovskite composition of
653 $\text{Rb}_{0.05}\text{Cs}_{0.05}[(\text{FA}_{0.83}\text{MA}_{0.17})]_{0.9}\text{Pb}(\text{I}_{0.83}\text{Br}_{0.17})_3$. The quadruple perovskite solution was
654 stirred for 6 at room temperature and then filtrated using a 0.45 μ m filter before use.
655 For RbCsMAFA film deposition, 50 μ L of the perovskite precursor solution was
656 spin-coated onto the substrates at 1000 and 5000 rpm for 10 and 20 s, respectively.
657 105 μ L chlorobenzene was dropped to the perovskite film at 25 s of the spinning
658 process. The perovskite films were then put on a hot plate at 100 $^{\circ}$ C for 60 min.

659

660 Preparation of $\text{MA}_{0.7}\text{FA}_{0.3}\text{PbI}_3$

661 The $\text{MA}_{0.7}\text{FA}_{0.3}\text{PbI}_3$ precursor solutions were contained 1.25 M
662 (PbI_2 :MAI:FAI=1:0.7:0.3) in a mixed solvent of DMF and DMSO (volume radio: 4:1).
663 12 mg $\text{Pb}(\text{SCN})_2$ (Sigma-Aldrich) was then added into 1mL $\text{MA}_{0.7}\text{FA}_{0.3}\text{PbI}_3$ precursor
664 solutions. For $\text{MA}_{0.7}\text{FA}_{0.3}\text{PbI}_3$ film deposition, 50 μ L of the perovskite precursor
665 solution was spin-coated onto the substrates at 1000 and 4000 rpm for 5 and 30 s,
666 respectively. 300 μ L chlorobenzene was dropped to the perovskite film at 13-15 s of
667 the spinning process. Then the as-deposited film was annealed at 65 $^{\circ}$ C for 2 min and
668 then 100 $^{\circ}$ C for 10 min.

669

670 Preparation of $\text{FA}_{0.8}\text{Cs}_{0.2}\text{Pb}(\text{I}_{0.7}\text{Br}_{0.3})_3$

671 The $\text{FA}_{0.8}\text{Cs}_{0.2}\text{Pb}(\text{I}_{0.7}\text{Br}_{0.3})_3$ precursor solutions were contained 0.8 M FAI, 0.2
672 M CsI, 0.55 M PbI_2 , 0.45 M PbBr_2 , and 0.55% M $\text{Pb}(\text{SCN})_2$ in a mixed solvent of
673 DMF and DMSO (volume radio: 3:1). For $\text{FA}_{0.8}\text{Cs}_{0.2}\text{Pb}(\text{I}_{0.7}\text{Br}_{0.3})_3$ film deposition, 50
674 μ L of the perovskite precursor solution was spin-coated onto the substrates at 1000
675 and 4000 rpm for 5 and 30 s, respectively. 300 μ L chlorobenzene was dropped to the
676 perovskite film at 13-15 s of the spinning process. The as-prepared film was annealed
677 at 65 $^{\circ}$ C for 2 min and then 100 $^{\circ}$ C for 10 min.

678

679 Preparation of $\text{Cs}_{0.03}(\text{FA}_{0.97}\text{MA}_{0.03})_{0.97}\text{Pb}(\text{I}_{0.97}\text{Br}_{0.03})_3$

680 The $\text{Cs}_{0.03}(\text{FA}_{0.97}\text{MA}_{0.03})_{0.97}\text{Pb}(\text{I}_{0.97}\text{Br}_{0.03})_3$ precursor solution was prepared
681 with the mixed powders of FAI: MABr: MACl: PbBr_2 : PbI_2 (molar ratio:
682 1.41:0.04:0.4:0.04:1.47) in the mixture of DMF: DMSO (4:1, v:v), blended with 3%
683 volume ratio of CsI (1.5 M) stock solution. For $\text{Cs}_{0.03}(\text{FA}_{0.97}\text{MA}_{0.03})_{0.97}\text{Pb}(\text{I}_{0.97}\text{Br}_{0.03})_3$
684 film deposition, 50 μ L of the perovskite solution was spin-coated onto the SnO_2
685 coated ITO substrate at 1000 and 6000 rpm for 10 and 30s, respectively. 150 μ L
686 chlorobenzene was dropped onto the perovskite film at 15-20 s of high-speed
687 spin-coating process. The as-prepared films were annealed at 120 $^{\circ}$ C for 1 h in the
688 ambient atmosphere with ~20% RH.

689

690 For Dimensionally Graded Passivation method, 100 μ L of BABr-IPA solution
(the concentrations ranged from 1 to 5 mg/mL) was spin-coated on the as-prepared

691 perovskite films at 5000 rpm for 30 s. Then the perovskite films were annealed at 100
692 °C for 10 min.

693 Perovskite solar cells fabrication

694 N-i-p solar cells: The indium tin oxide (ITO)-coated glass was sequentially
695 cleaned using deionized water, acetone, and ethanol. All substrates were further
696 cleaned by UV-ozone for 15 min before deposition of SnO₂ ETL. 30 nm SnO₂ QD
697 ETL was deposited on the cleaned ITO substrate by spin-coating as-prepared colloidal
698 SnO₂ QD solution.¹⁴ Following, the as-deposited SnO₂ QD ETL was annealed on a
699 hot plate at 200 °C for 1 h in air. The mixed-cation perovskite was deposited via a
700 one-step spin-coating procedure as mentioned above. 20 μL spiro-OMeTAD solution
701 containing 72.3 mg spiro-OMeTAD (Lumitech), 28.8 μL tert-butylpyridine (t-BP,
702 Sigma-Aldrich), 17.5 μL bis(trifluoromethanesulfonyl)imide (Li-TFSI, Sigma-Aldrich)
703 solution (520 mg in acetonitrile), and 1 mL chlorobenzene was spin-coated onto the
704 perovskite layer at 3000 rpm for 20 s. Finally, a thickness of 80 nm Au was deposited
705 by thermal evaporation.

706 P-i-n solar cells: The PTAA solution (2 mg/mL in toluene) was spin-coated onto
707 the perovskite layer at 5000 rpm for 30s and annealed at 100 °C for 10 min. 1.63 eV
708 perovskite layer was deposited on PTAA layer with the same method based on
709 one-step approach. Then, 30-nm-thick C₆₀ layer (electron transport layer) and
710 12-nm-thick SnO₂ layer (buffer layer) were deposited by thermal evaporation and
711 atomic layer deposition, respectively. Finally, 100-nm-thick Cu was thermal
712 evaporated as top metal electrode.

713

714 Solar cell characterization

715 The current-voltage (*J-V*) characteristics of the devices were measured by using a
716 Keithley 2400 Source Meter under standard AM 1.5 G Simulator (SS-F5, Enli
717 Technology Co. Ltd., Taiwan), and the light intensity was calibrated by a standard
718 SRC-2020 Si reference cell. The *J-V* curves were obtained from the range of 1.3 V to
719 -0.1 V with a scan speed of 100 mV/s from both reverse and forward scan direction.
720 The active area of device is 0.09 cm², a mask with an aperture area of 0.0625 cm² was
721 used to define device area. The stabilized output of the devices was measured by
722 recording the current output of the illuminated device while holding it at a constant
723 voltage near the maximum power point extracted from the *J-V* curve.

724 Solar cell certification

725 Device certification was conducted by Enli Tech. Optoelectronic Calibration Lab.,
726 a photovoltaic certification laboratory accredited by Taiwan Accreditation Foundation
727 (Accreditation Criteria: ISO/IEC 17025:2005).

728

729 Photo-stability test

730 The devices are kept under a white light-emitting diode (LED) array with 0.8 sun
731 intensities, which was calibrated using a standard silicon solar cell (KG 5). The
732 encapsulated devices were exposed to below 20% relative humidity at ~35 °C.

733

734 External quantum efficiency (EQE)

735 The EQE measurements of photovoltaic device were carried out from 300 to 850
736 nm using a QE-R 3011 system (Enli Tech, Taiwan).

737

738 X-ray diffraction (XRD) and Grazing-incidence wide-angle X-ray scattering
739 (GIWAXS) characterization

740 The crystal structure and phase of the materials were characterized using an XRD
741 (Rigaku SmartLab X-ray diffractometer) with Cu K α radiation under operation
742 conditions of 40 kV and 40 mA (The θ -2 θ scan mode from 10° to 70° in a step of
743 0.01°). The GIWAXS measurements were carried out with a Xeuss 2.0 SAXS/WAXS
744 laboratory beamline using a Cu X-ray source (8.05 keV, 1.54 Å) and a Pilatus3R
745 300K detector. The incidence angle is 0.3°. The perovskite films for XRD and
746 GIWAXS characterizations were deposited on on SnO₂-coated ITO substrates.

747

748 Scanning electron microscopy (SEM)

749 The morphologies and microstructures were investigated by using a TESCAN
750 MAIA₃ field emission scanning electron microscopy. The perovskite films for SEM
751 measurement were prepared on SnO₂-coated ITO substrates.

752

753

754 Atomic force microscopy (AFM)

755 Bruker NanoScope 8 atomic force microscope was used to measure height and
756 phase profile of perovskite films in the tapping mode. The perovskite films for AFM
757 measurement were prepared on SnO₂-coated ITO substrates.

758

759 Photothermal deflection spectroscopy (PDS)

760 For PDS measurement, the perovskite film was deposited on quartz substrate and
761 then immersed into Fluorinert FC-72 from 3M Corporation. A monochromatic light
762 beam was modulated at 13 Hz by a mechanical chopper to excite the perovskite films
763 from the quartz side. A laser was at the perpendicular side so that it was deflected
764 periodically. A position detector, connected with a lock-in amplifier, was placed on the
765 other side so that the beam deflection signal was measured.

766

767 The time-of-flight secondary-ion mass spectroscopy (ToF-SIMS)

768 The perovskite films were deposited on the ITO substrates for ToF-SIMS
769 measurement. The ToF-SIMS measurements (Model TOF-SIMS V, ION-TOF GmbH)
770 were conducted with the pulsed primary ions from a Cs⁺ (3 keV) liquid-metal ion gun
771 or C₆₀ (10 keV) for the sputtering and a Bi⁺ pulsed primary ion beam for the analysis
772 (25 keV).

773

774 Time-resolved photoluminescence and photoluminescence spectra

775 Photoluminescence measurements of perovskite film on glass were conducted by
776 using an Edinburgh FLSP920 spectrophotometer installed with the excitation source
777 of 485 nm picosecond pulsed diode laser in the average power of 0.15 mW.

778

779 Ultraviolet-visible (UV-Vis) absorption spectra

780 The absorption spectra of the perovskite films were measured by an UV-vis
781 spectrophotometer (CARY5000, Varian, Australia) in a wavelength range at 300-850
782 nm at room temperature.

783

784 Ultraviolet photoelectron spectroscopy (UPS)

785 The samples for UPS measurements were made by depositing perovskite films on
786 the ITO conductive substrates. Then the UPS measurement was performed using a
787 XPS/UPS system (Thermo Scientific, Escalab 250Xi).

788

789 Photoluminescence quantum efficiency (PLQE)

790 The PLQE of perovskite films was measured using an integrating sphere
791 (Edinburgh instruments) with a 485-nm excitation laser ($\sim 125 \text{ mW/cm}^2$) in open-air
792 conditions.

793

794 External quantum efficiency of the electroluminescence (EQE_{EL})

795 The EQE_{EL} of the solar cells was determined by measuring the emitted photons of
796 devices in all directions through an integrated sphere by using a calibrated
797 spectrometer (QE Pro, Ocean Optics), under a constant current density provided by a
798 Keithley 2400 source measure unit. The devices were left at room temperature in
799 open-air conditions.

800

801 Trap density of states (tDOS)

802 Admittance spectra were measured by using an Agilent E4980A meter with an
803 alternating voltage of 20 mV. The frequency-dependence of the capacitance was
804 recorded from 1 kHz to 2000 kHz with zero bias in the dark.

805

806 Transmission electron microscope characterization (TEM)

807 Transmission electron microscopy (TEM) lift-out samples were prepared via
808 focused ion beam (FIB) polishing in a TESCAN GAIA3 FIB-SEM. A covering layer
809 of 1.5 μm thick platinum was deposited by electron beam. The TEM lamella was
810 extracted by FIB with an ion beam of accelerating voltage of 30 kV and current of 7
811 nA and welded to a TEM copper grid by platinum. After that, the TEM lamella was
812 polished to about 300 nm thick with accelerating voltage of 30 kV and current of 100
813 pA. Finally, it was thinned to electron transparency with accelerating voltage of 5 kV
814 and current of 25 pA and accelerating voltage of 2 kV and current of 20 pA.
815 Accelerating voltage for SEM observation and electron beam deposition was kept at 5
816 kV during the whole process. The TEM lift-out sample was sent into TEM chamber in
817 less than one minute after the sample preparation. TEM observations were carried out
818 by using a JEOL ARM200CF transmission electron microscope equipped with a cold
819 field-emission electron gun and double spherical-aberration correctors (CEOS GmbH)
820 operated at 80 kV.

821

822 Density functional theory (DFT) calculations

823 All the calculations were performed based on the DFT calculations using Vienna ab
824 initio simulation package (VASP) code with the standard frozen-core projector
825 augmented-wave (PAW) method. The generalized gradient approximation (GGA) of
826 Perdew-Burke-Ernzerh (PBE) function is employed for exchange-correlation
827 potential. The cut-off energy for basis functions is 400 eV and the k-point mesh was
828 obtained using the Monkhorst-Pack method with a reasonable grid density. Atoms are
829 fully relaxed until the Hellmann-Feynman forces on them are 0.01 eV/Å and the
830 vacuum layer is 15Å, which is long enough to reach the calculation precision. The
831 effect of van der Waals interactions was considered by using the empirical correction
832 method proposed by Grimme (DFT-D3) with the Becke and Johnson (BJ)-damped.
833 Dipole correction was applied to compensate for the dipole interaction.

834

835

836

837

838

839

840

841

842

843

844

845

846

847

848

849

850

851

852

853

854

855

856

857

858

859

860

861

862

863

864

865

866

867
868
869
870
871
872
873
874
875
876
877
878
879
880
881
882
883
884
885
886
887
888
889
890
891
892
893
894
895
896
897
898
899
900
901
902
903
904
905
906
907
908

Figure 1 | Device architecture and ToF-SIMS profiling of DGPF devices. a, b, A schematic diagram (a) and cross-sectional TEM images (b) of our fabricated DGPF film deposited on the SnO₂-coated ITO substrate. **c,** TOF-SIMS depth profiles of DGPF perovskite films deposited on ITO substrates.

909
910
911
912
913
914
915
916
917
918
919
920
921
922
923
924
925
926
927
928
929
930
931
932
933
934
935
936
937
938
939
940
941
942
943
944
945
946
947

Figure 2 | Crystallinity and Morphology of perovskite films. **a**, 2D GIWAXS patterns of control and DGPF perovskite films with various concentrations of BABr solution (BABr concentrations: 0 mg/ml, 1 mg/ml, 2 mg/ml, and 5 mg/ml). **b**, Radial intensity profiles averaged over the entire 2D GIWAXS image. **c**, Intensity profiles along the q_z axis. **d**, Schematic of formed 2D/3D perovskite films via DGPF method, in which a thin 2D perovskite capping layer with mixed-dimensionality was formed on top of 3D perovskite films, and 2D perovskite phase can be further produced between the grain boundaries of the 3D counterparts leading to the formation of mixed 2D/3D perovskite. **e**, Top view SEM and surface AFM images of control and DGPF perovskite films with different BABr concentrations.

948
949
950
951
952

953
954
955
956
957
958
959
960
961
962
963
964
965
966
967
968
969
970
971
972
973
974
975
976
977
978
979
980
981
982
983
984
985

Figure 3 | Photovoltaic performance and optoelectronic properties of perovskite solar cells. **a**, *J-V* curves obtained from forward and reverse scan directions for the champion PSC device based on 1.63 eV perovskite composition. **b**, External quantum efficiency, and the electroluminescence (EL) spectra for control and DGPF-based perovskite devices. **c**, Calculated EL quantum efficiency derived from the EL spectra at an injection current density of 22 mA/cm² (Here, the measured V_{OC} of control (0-BABr) and DGPF (2-BABr) PSCs are 1.16 V and 1.23 V, respectively). **d**, *J-V* curves of the champion control and DGPF based devices in a ~1.53 eV perovskite system from forward and reverse scan directions. **e**, EQE spectrum of the DGPF based device with an integrated J_{SC} of 24.25 mA/cm². **f**, EQE_{EL} as a function of the injection current density for the control and DGPF based PSCs when operating as LEDs.

986
987
988
989
990
991
992
993
994
995
996
997
998
999
1000
1001
1002
1003
1004
1005
1006
1007
1008
1009
1010
1011
1012
1013
1014
1015
1016
1017
1018
1019
1020
1021
1022
1023
1024
1025
1026

Figure 4 | Operational stability of control and DGPF devices. Device Stability parameters of control and DGPF perovskite devices with encapsulation. Data obtained from current density-voltage scans over time for devices. **a**, N-I-P devices are kept under a white light-emitting diode (LED) array with 0.8 sun intensities under open-circuit (OC) condition (20-30% RH, 35-40 °C). **b**, The stability data were determined from maximum power point tracking of P-I-N devices illuminated at 1-sun irradiation by LED lamp in ambient condition (30-40% RH, 60-65 °C).

1027

1028

1029

1030

1031

1032

1033 **Table 1.** Photovoltaic parameters and voltage loss analysis of the best-performing

1034 PSCs

1035

1036

1037

1038

1039

1040

1041

1042

1043

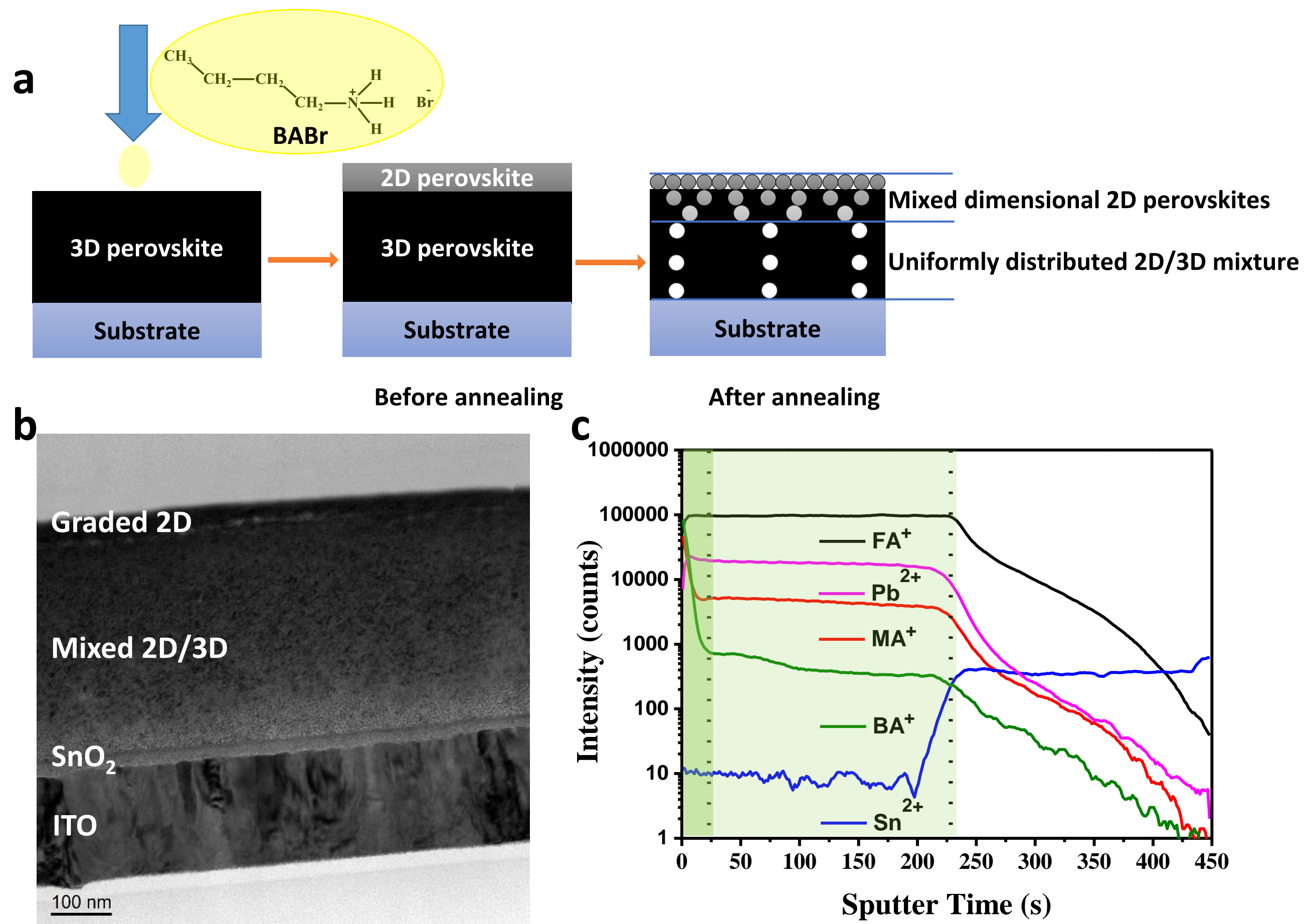


Figure 1

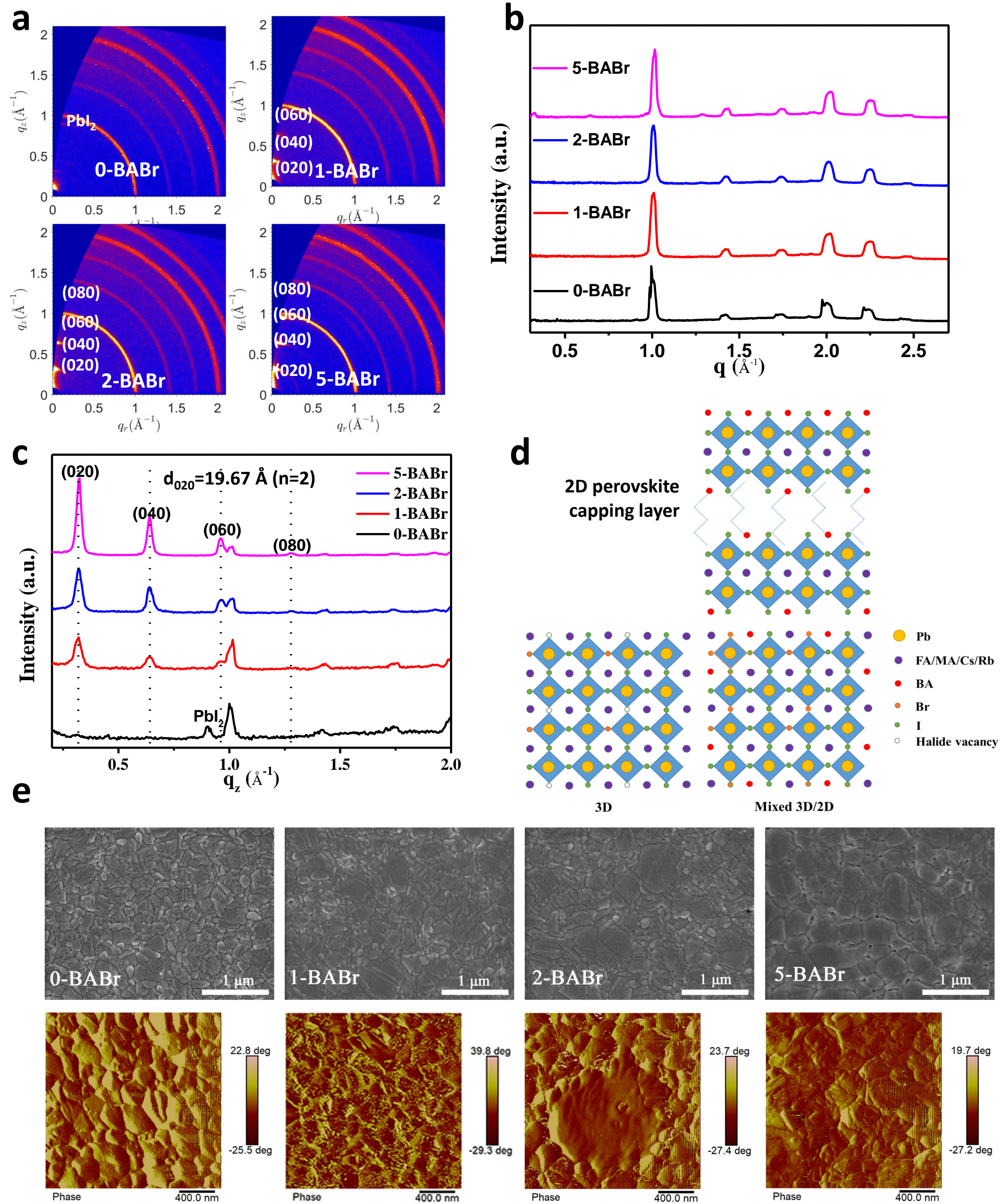


Figure 2

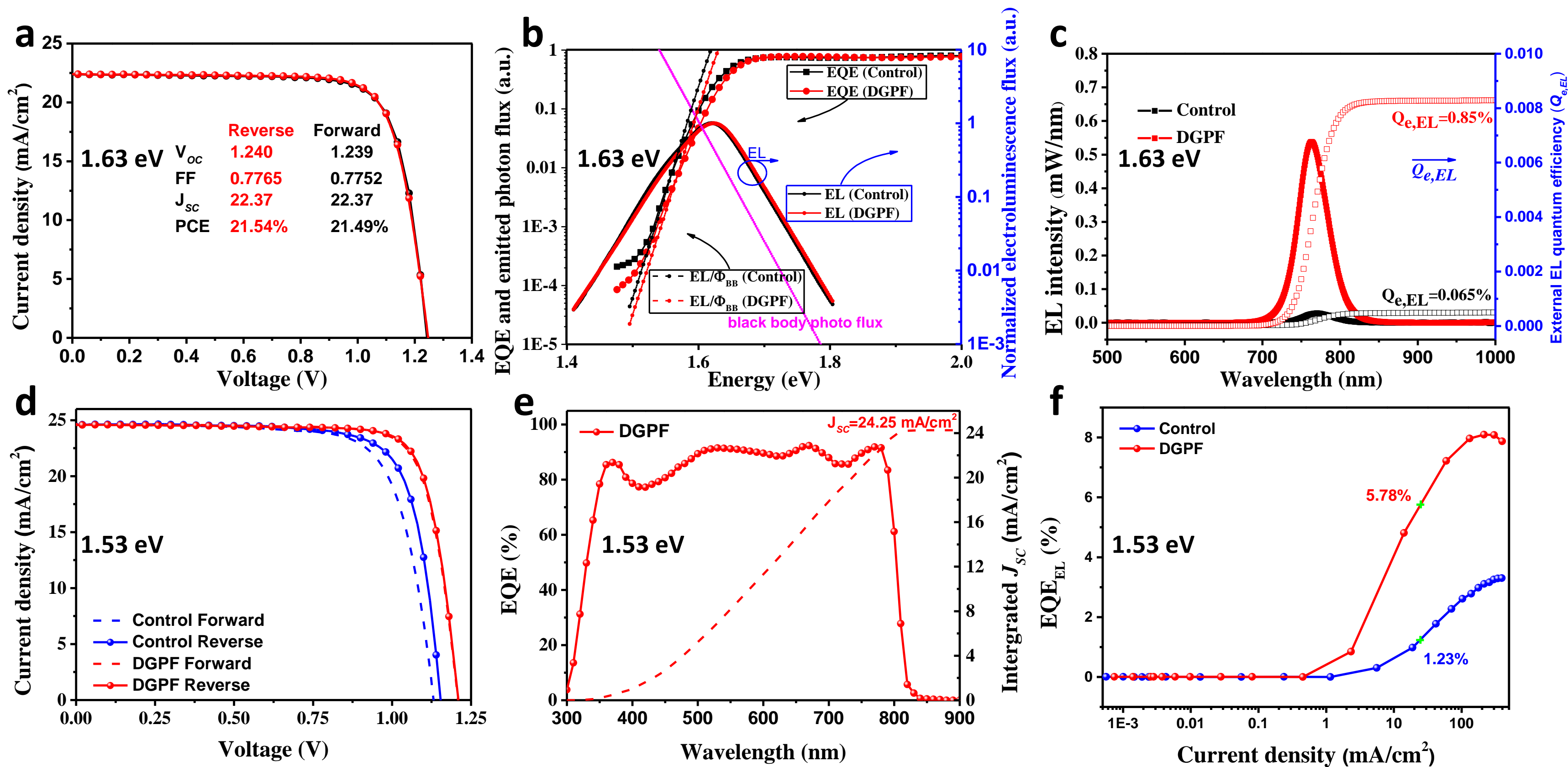


Figure 3

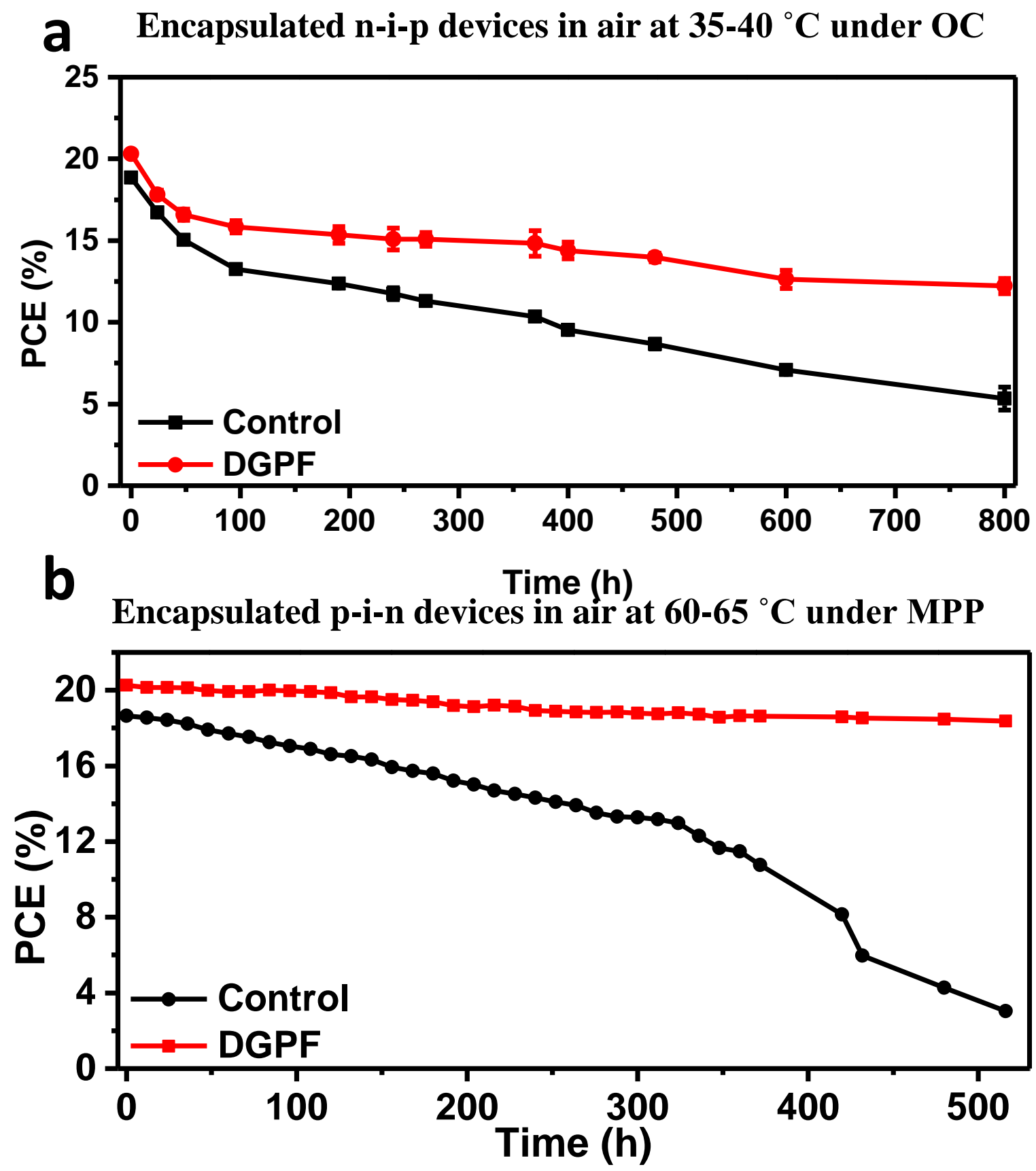


Figure 4

Perovskite composition	Conditions	E_g^a (eV)	V_{OC} (V)	J_{SC} (mA cm ⁻²)	FF (%)	PCE (%)	$\Delta V_{OC,SQ}^b$ ($\Delta V_{OC,rad}^c$) (V)	$\Delta V_{OC,nr}^d$ (V)
MA _{0.7} FA _{0.3} PbI ₃	Control	1.555	1.094	22.68	74.77	18.58	0.273	0.188
	DGPF	1.561	1.160	22.95	77.57	20.67	0.273	0.128
RbCsMAFA (I:Br=0.83:0.17)	Control	1.628	1.161	22.25	75.92	19.61	0.283	0.184
	DGPF	1.632	1.240	22.37	77.65	21.54	0.283	0.109
FA _{0.8} Cs _{0.2} Pb(I _{0.7} Br _{0.3}) ₃	Control	1.733	1.212	18.24	73.21	16.18	0.285	0.236
	DGPF	1.737	1.260	18.44	77.82	18.08	0.285	0.192
Cs _{0.03} (FA _{0.97} MA _{0.03}) _{0.97} Pb(I _{0.97} Br _{0.03}) ₃	Control	1.533	1.154	24.60	76.50	21.71	0.272	0.107
	DGPF	1.536	1.210	24.57	80.00	23.78	0.272	0.054

Note:

^a E_g was derived from the average value of E_g^{IP} and E_g^{Tauc} .

^b $\Delta V_{OC,SQ}$ was calculated (as a function of bandgap) using detailed balance principle.

^c $\Delta V_{OC,rad}=Eg/q-V_{OC,rad}$, and this is only available for 1.63 eV perovskites shown in this table.

^d $\Delta V_{OC,nr}$ was calculated from W_{OC} and $\Delta V_{OC,SQ}$ or $\Delta V_{OC,rad}$.